Logic-based mechanistic machine learning on high-content images reveals how drugs differentially regulate cardiac fibroblasts

Anders R. Nelson[1], Steven L. Christiansen[1,2], Kristen M. Naegle[1], Jeffrey J. Saucerman[1*]

1) University of Virginia School of Medicine, Charlottesville, VA 22903

2) Brigham Young University Department of Biochemistry, Provo, UT 84602

*University of Virginia School of Medicine, Charlottesville, VA 2290

(e-mail: jsaucerman@virginia.edu)

PO Box 800759, Charlottesville, VA 22908, 434-924-5095

Classification: Biological Sciences; Systems Biology

Keywords: Fibrosis, Fibroblast, Machine learning, Cell Biology, Differentiation, Drugs

Abstract

Fibroblasts are essential regulators of extracellular matrix deposition following cardiac injury. These cells exhibit highly plastic responses in phenotype during fibrosis in response to environmental stimuli. Here, we test whether and how candidate anti-fibrotic drugs differentially regulate measures of cardiac fibroblast phenotype, which may help identify treatments for cardiac fibrosis. We conducted a high content microscopy screen of human cardiac fibroblasts treated with 13 clinically relevant drugs in the context of TGFβ and/or IL-1β, measuring phenotype across 137 single-cell features. We used the phenotypic data from our high content imaging to train a logic-based mechanistic machine learning model (LogiMML) for fibroblast signaling. The model predicted how pirfenidone and Src inhibitor WH-4-023 reduce F-actin assembly and F-actin stress fiber formation, respectively. Validating the LogiMML model prediction that PI3K partially mediates the effects of Src inhibition, we found that PI3K inhibition reduces F-actin fiber formation and procollagen I production in human cardiac fibroblasts. In this study, we establish a modeling approach combining the strengths of logic-based network models and regularized regression models, apply this approach to predict mechanisms that mediate the differential effects of drugs on fibroblasts, revealing Src inhibition acting via PI3K as a potential therapy for cardiac fibrosis.

Significance

Cardiac fibrosis is a dysregulation of the normal wound healing response, resulting in excessive scarring and cardiac dysfunction. As cardiac fibroblasts primarily regulate this process, we explored how candidate anti-fibrotic drugs alter the fibroblast phenotype. We identify a set of 137 phenotypic features that change in response to drug treatments. Using a new computational modeling approach termed logic-based mechanistic machine learning, we predict how pirfenidone and Src inhibition affect the regulation of the phenotypic features F-actin assembly and F-actin stress fiber formation. We also show that inhibition of PI3K reduces F-actin fiber formation and procollagen I production in human cardiac fibroblasts, supporting a role for PI3K as a mechanism by which Src inhibition may suppress fibrosis.

Introduction

Cardiac fibroblasts are the primary regulators of remodeling following cardiac injury[1]. Extracellular matrix (ECM) deposition by activated myofibroblasts is essential to this response, but excessive deposition can lead to ventricular stiffness, diastolic dysfunction, and heart failure[1]. While fibroblasts are critical to the wound healing response, current standard-of-care

therapeutics for cardiac injury, such as myocardial infarction (MI), affect downstream symptoms but do not specifically target fibroblast signaling[2]. Recent drug discovery and development has focused on identifying drugs such as Entresto (sacubitril/valsartan) that reduce fibrosis in part by modulating fibroblast signaling[3,4].

Collagen secretion, αSMA expression, and F-actin assembly are traditional markers for a profibrotic fibroblast phenotype[5,6]. While high expression of these markers provides an initial indication of myofibroblast activation, traditional marker expression is inconsistent and does not fully capture the fibrotic response[7]. Recent studies of fibroblast phenotype have shown that fibroblasts exhibit high phenotypic heterogeneity across many facets in response to injury, and that phenotypic changes are also sensitive to drug perturbations[8–11]. Identifying drugs that regulate fibroblast signaling may provide targeted control of fibrosis.

Previously, we developed a logic-based mechanistic network model of fibroblast signaling and applied it to perform virtual screens for anti-fibrotic drugs[12,13]. That study predicted and experimentally validated an antifibrotic role for the TGFβ receptor inhibitor galunisertib[13]. While the fibroblast network model predicts a number of drugs that modulate fibroblast activation, substantial experimental characterization is needed to capture phenotypic responses to drugs that were not captured by prior modeling.

In this study, we combined high content microscopy, network modeling, and machine learning to identify drugs that differentially regulate fibroblast phenotypic metrics and predict their underlying network mechanisms. We used image-based feature extraction to more deeply characterize drug response and fibroblast phenotype, capturing drug-induced changes across a set of single-cell metrics relevant to fibrosis. Using a novel logic-based mechanistic machine learning approach, LogiMML, we predicted signaling pathways that determine how drugs regulate fibroblast phenotype. Finally, we experimentally validated the main pathway mechanism predicted by the LogiMML model that mediates how Src inhibition suppresses fibrotic responses.

Results

An *in vitro* screen for candidate fibrosis drugs

Previously, we applied our published cardiac fibroblast network model[12] to identify candidate therapies predicted to reduce cardiac fibrosis[13]. This logic-based differential equation network model was developed from a wide range of fibroblast signaling relationships from *in vitro* studies in the literature. The model predicts changes in fibrotic outputs including collagen I and III, αSMA, EDA fibronectin, matrix metalloproteases, and F-actin in response to changes in extracellular signaling contexts and drug treatment[12]. This model was previously integrated with the drug-target database DrugBank to make predict the response of fibroblasts to 121 FDA-approved or investigational drugs that have targets in this network[13].

102 To expand upon the *in silico* modeling work done in that previous study[13], we aimed to develop
103 a list of drug candidates to test experimentally for their ability to reduce fibrosis in cardiac
104 fibroblasts *in vitro*. As the model predicted many drugs to reduce fibrosis effectively[13], we
105 included drug selection criteria outside of our modeling results alone to further narrow-down a
106 list of candidate drugs. First, we prioritized pathway diversity of the drug targets to ensure that
107 we would perturb fibrotic signaling comprehensively and avoid testing redundant drugs in our
108 experiments. As drug repurposing has become an increasingly effective and efficient strategy
109 for treating cardiovascular disease, we next looked to prioritize drugs that had previous clinical
110 indications for other disease areas[14,15]. Using these criteria, we selected thirteen drugs to
111 evaluate experimentally: anakinra, valsartan, defactinib, HW-4-023, glutathione, CW-HM12,
112 salbutamol, marimistat, fasudil, SB203580, pirfenidone, brain natriuretic peptide (BNP), and a
113 combination of valsartan and BNP (Table S1). Among the list of candidate drug targets are
114 regulators for inflammatory signaling, mechanical stretch response, non-canonical TGFβ
115 signaling, and modification of secreted proteins.

116 We next aimed to test these candidate drugs for their ability to quantitatively reduce fibrosis as
117 characterized by image-based single-cell profiling of procollagen I, α-smooth muscle actin
118 (αSMA), and F-actin. In injury signaling conditions, such as following myocardial infarction (MI),
119 myocardial cells are exposed to elevated proinflammatory and profibrotic stimuli[16–18]. To
120 represent these signaling contexts in an *in vitro* system, we included IL1β and TGFβ, shown to
121 be elevated following cardiac injury, in our treatment conditions to represent proinflammatory
122 and profibrotic contexts respectively[19–21]. We tested our candidate drugs under four total
123 cytokine contexts (baseline context with no added cytokine, fibrotic context represent by TGFβ,
124 inflammatory context represented by IL1β, and combined context represent by both TGFβ and
125 IL1β)[19–21]. In total, we used 108 treatment conditions consisting of one of the thirteen drugs at
126 a low, medium, or high dose combined with one of the four cytokine contexts. We also included
127 treatments of each cytokine context with no drug to establish a control baseline for cell
128 responses to cytokines. We imaged and quantified single-cell protein expression of three
129 fibrotic markers, procollagen I, α-smooth muscle actin (αSMA), and F-actin using high-content
130 microscopy and a custom CellProfiler software pipeline[22].

131 Interestingly, the antifibrotic drugs in our screen induced differential effects on fibrosis. Of the
132 13 candidate drugs, WH-4-023, fasudil, and defactinib caused the strongest reduction of
133 procollagen I, F-actin, and αSMA expression in a TGFβ signaling context, even at the lowest
134 dose (Figure 1A). Conversely, a second set of drugs including anakinra and glutathione
135 increased fibrotic marker expression in both TGFβ and combined TGFβ/IL1β contexts when
136 applied directly to fibroblasts. In a previous clinical study, anakinra, an IL1 receptor inhibitor,
137 was shown to improve cardiac function and reduced heart failure incidence following acute MI
138 in human patients[23]. While anakinra has been shown to reduce infarct scar area in a mouse MI
139 model, it also exhibits other beneficial cardiac effects post-MI including inhibition of post-MI
140 myocyte apoptosis and reduction in systemic inflammation[24,25]. Based on these previous
141 studies, it is likely that anakinra has a net antifibrotic effect on fibroblasts in the presence of

142 other myocardial cell types even though anakinra treatment increased fibrotic marker
143 expression in this experiment. A third set of drugs showed more selective antifibrotic effects.
144 For example, while fasudil significantly reduced expression of all three fibrosis markers in a
145 TGFβ signaling context, pirfenidone only significantly reduced F-actin (Figure 1 B-E). This third
146 set of drugs is of particular interest as it contains drugs that differentially regulate markers for
147 fibrosis. Given the recent clinical effectiveness of pirfenidone for lung fibrosis, and success in
148 diseases models for cardiac fibrosis[26,27], we further investigated the mechanisms by which it
149 regulates F-actin in cardiac fibroblasts.

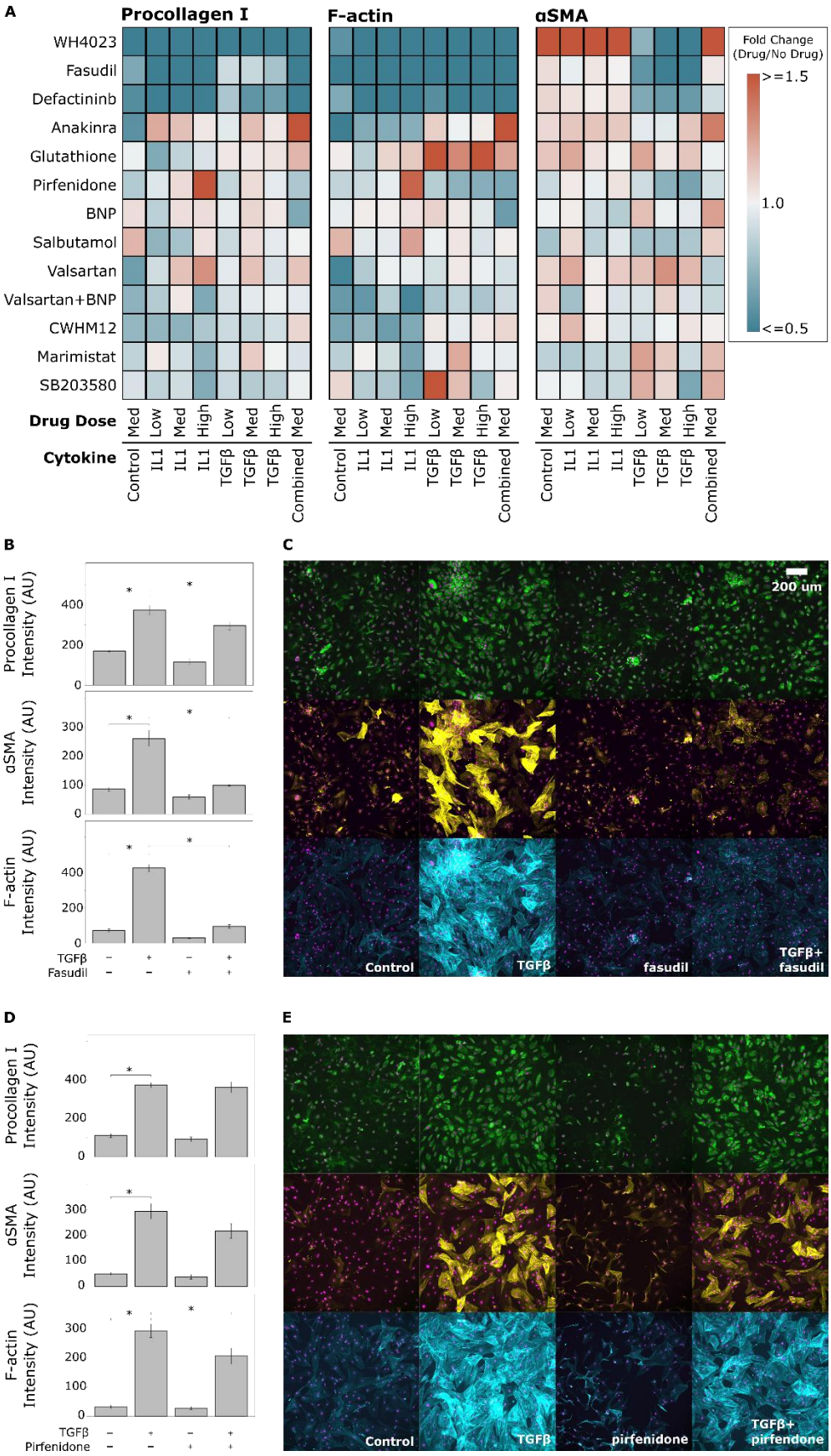
A
Procollagen I
F-actin
αSMA
WH4023
Fasudil
Defactininb
Anakinra
Glutathione
Pirfenidone
BNP
Salbutamol
Valsartan
Valsartan+BNP
CWHM12
Marimistat
SB203580
Drug Dose
Cytokine
Med
Low
High
Control
IL1
TGFβ
Combined
Fold Change (Drug/No Drug)
>=1.5
1.0
<=0.5
B
Procollagen I Intensity (AU)
αSMA Intensity (AU)
F-actin Intensity (AU)
TGFβ
Fasudil
C
200 um
Control
TGFβ
fasudil
TGFβ+ fasudil
D
Pirfenidone
E
pirfenidone
TGFβ+ pirfendone

Figure 1: **High-content microscopy screen for drugs that module fibroblast activation.** A) Expression of fibroblast activation markers procollagen I, F-actin, and αSMA in human cardiac fibroblasts upon treatment of 13 drugs at 3 doses, under environmental contexts of TGFβ, IL1β, or both. Fold change values show 'drug vs. no drug' Integrated Intensities for each protein. Panels B and C show quantification and representative images of the effects of pirfenidone, a non-specific inhibitor of TGFβ expression, which consistently regulates fibrotic protein expression. Panels D and E show quantification and representative images of the effects of fasudil, a Rho-kinase inhibitor, which differentially regulates fibrotic protein expression. *p≤0.05 ANOVA with Tukey's post-hoc.

151

152 LogiMML: logic-based mechanistic machine learning model predicts how drugs regulate 153 fibroblast phenotype

154 Assembled F-actin filaments play a key role in contractility as fibroblasts transition to become
155 myofibroblasts[28]. Therefore, we asked whether the previous mechanistic computational model
156 of the fibroblast signaling network[12] could predict our experimentally measured inhibition of F-
157 actin by pirfenidone from Figure 1D. While the model had correctly predicted responses to a
158 number of drugs including galunisertib[13], here, the original mechanistic model did not capture
159 the ability of pirfenidone to suppress F-actin in a TGFβ signaling context (Figure 2 A).

160 Given the limitations of a model based only on prior knowledge, we asked whether drug
161 predictions could be improved by combining the mechanistic model with a machine learning
162 model that leverages data from the drug screen. Motivated by 'white-box' machine learning
163 strategies that combine mechanistic models with machine learning[29,30], we designed a logic-
164 based mechanistic machine learning (LogiMML) model to predict key regulators that conduct
165 signaling from network model inputs and simulated drugs to experimentally measured
166 phenotypic outputs (Figure 2 B). As the 108 treatments were insufficient to infer new links to
167 phenotypic outputs from all 91 model nodes, we reduced the model's dimensionality by
168 clustering nodes into modules. Eleven signaling modules were computed based on a combined
169 influence and sensitivity analysis, grouping nodes with similar predicted behavior across
170 signaling contexts. The machine learning component was then trained by mapping the model-
171 predicted activity of each network module for each of the 108 drug+cytokine treatments to
172 respective experimentally measured outputs. Regularized ridge regression was selected for the
173 machine learning layer of the LogiMML model to reduce the likelihood of overfitting[31]. As
174 measured experimentally, the LogiMML model correctly predicted the respective induction and
175 suppression of F-actin by TGFβ and pirfenidone (Figure 2 C).

176 We next asked whether the LogiMML model could provide new mechanistic insights into how
177 F-actin is regulated by pirfenidone. First, we used the LogiMML model's ridge regression
178 coefficients to predict the modules that most influence F-actin. 'PI3K' and 'Smad3' modules
179 were predicted to be the top positive regulators of F-actin, while the 'P38_Calcium' module was
180 predicted as the top negative regulator (Figure 2 E). These predictions for fibroblasts are
181 consistent with previous studies with other cell types showing that members of the 'Smad3'

182 and ‘P38_Calcium’ signaling modules regulate F-actin filament assembly in endothelial cells and

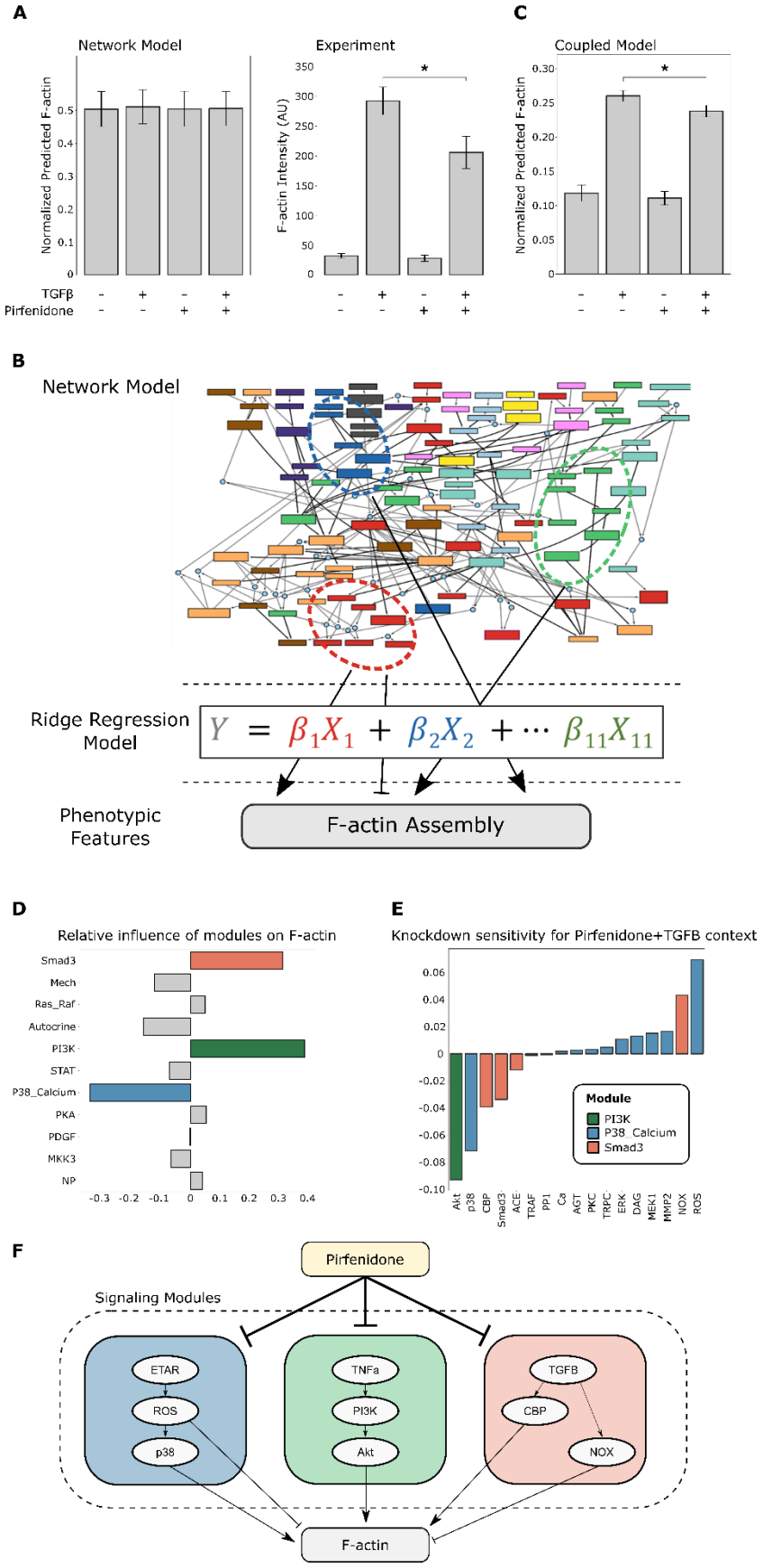

Figure 2: **LogiMML logic-based mechanistic machine learning approach guides model revision and predicts network mechanisms underlying pirfenidone suppression of F-actin.** A) Original fibroblast network model predicts no change in F-actin upon TGFβ or pirfenidone treatment. Experimental data shows pirfenidone significantly reverses the increase of F-actin by TGFβ (data previously shown in figure 1 D). B) Schematic of the LogiMML approach for integrating logic-based network modeling with machine learning to predict network mechanisms for cell phenotypes. The average activity within each network module is mapped to predict fibroblast phenotypic features via a Ridge regression layer. C) The Coupled LogiMML model predicts TGFβ and pirfenidone effects on F-actin that qualitatively match experimental data shown in panel A. D) LogiMML ridge regression coefficients show predicted relative influence of network modules on F-actin. E) LogiMML node knockdown sensitivity analysis in the context of TGFβ+pirfenidone. Nodes from most influential modules are sequentially knocked down, predicting change in F-actin upon knockdown. F) Schematic of the network mechanisms predicted for the actions of pirfenidone on F-actin, derived from sensitivity analysis in panel E.

183 that members of the 'PI3K' signaling module promote actin filament remodeling during
184 migration in embryonic fibroblasts [32–34]. To identify which individual signaling nodes within
185 these three modules most regulate F-actin, we performed a virtual knockdown screen of the
186 LogiMML model for regulators of F-actin in a 'TGFβ+pirfenidone' signaling context (Figure 2 E).
187 Summarizing these analyses, the LogiMML model predicts that pirfenidone regulation of F-actin
188 is positively regulated by p38, Akt, and CBP, while negatively regulated by ROS and NOX (Figure
189 2 F).

190

191 Drugs and pathways controlling fibroblast morphology and texture

192 Given the differential regulation of fibrosis marker protein expression, we asked whether other
193 aspects of fibroblast phenotype may also be differentially regulated by drugs and cytokines.
194 Qualitatively, we observed morphological changes in cell shape, stress fiber formation,
195 intracellular protein distribution, and cell area (e.g. for pirfenidone treatment see Figure 1 E).
196 To measure these characteristics of fibroblast phenotype, we developed a custom CellProfiler
197 image analysis pipeline quantifying 137 total single-cell cell features[22,35]. Integrated intensities
198 for the three fibrotic marker proteins, procollagen I, F-actin, and αSMA clustered relatively
199 close to each other across the feature space (Figure 3 A). As expected, expression of these
200 marker proteins and similar features were high under TGFβ and TGFβ-like treatments, and low
201 under negative control and IL1β conditions. While the central rows of the heatmap contain
202 many features with similar treatment responses, the features at the top and bottom regions of
203 the heatmap show high heterogeneity in response to drugs.

204 To gain a comprehensive understanding of fibroblast phenotypic responses to drugs and
205 cytokines, we applied principal component analysis (PCA) dimensionality reduction to the data
206 (Figure 3 B-C). To mitigate feature redundancy and improve PCA performance, we first reduced
207 the feature set from 137 total features to 18 representative features. These features were

208 selected by clustering a correlation matrix of the feature set into 15 clusters, selecting one
209 feature from each cluster (Figure S1, Figure S2) as key representatives of that cluster's
210 information. The three integrated intensity features for procollagen I, F-actin, and αSMA were
211 also retained.

212 Negative control treatments had a negative score on the first principal component (PC1), while
213 cells treated with TGFβ showed a high positive score on PC1, indicating that the first principal
214 component correlates with an axis of classical fibroblast activation (Figure 3 B, Figure S3 A). This
215 was further supported by the PCA loading values for integrated procollagen I, F-actin, and
216 αSMA (Figure 3 C, Figure S3 B). These three features are expected to be relatively high in
217 activated myofibroblasts and indeed have strong positive loadings on PC1. On the PCA scores,

218 any of the 'TGFβ + Drug' groups deviated from the control-TGFβ axis defined on PC1, implying

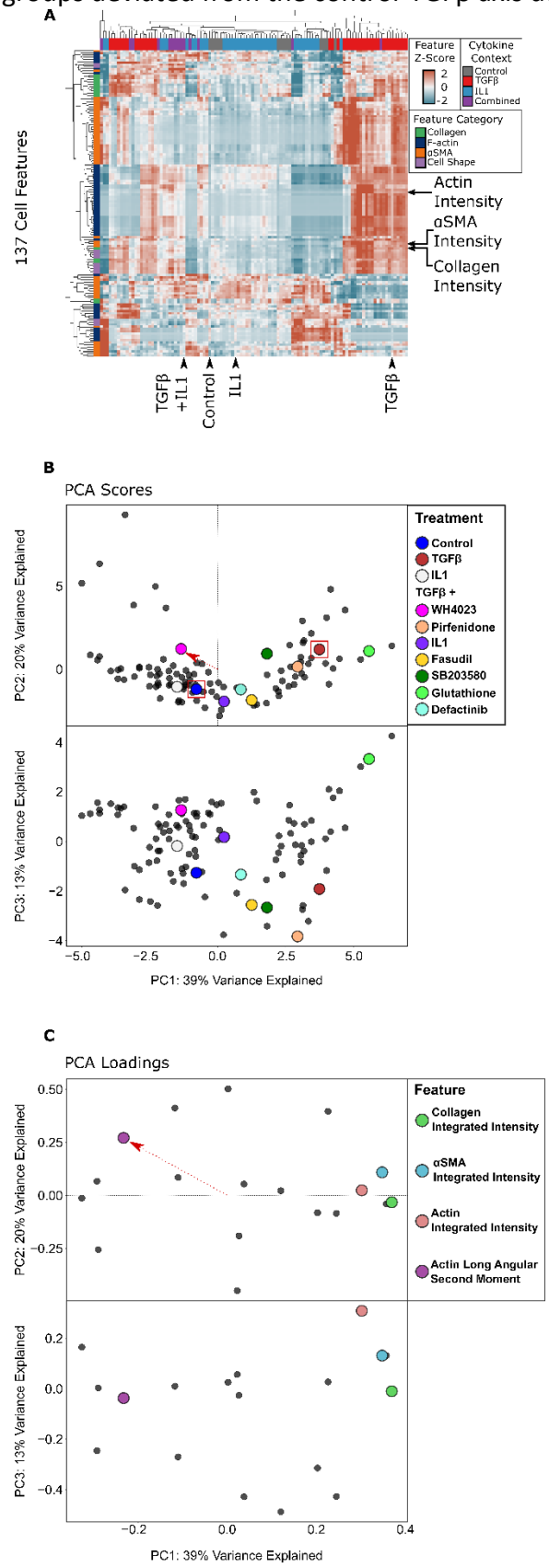

Figure 3: **Survey of single-cell fibroblast phenotypic features in response to 13 drugs at 3 doses and 4 environmental contexts.** A) 137 single-cell fibroblast features that quantify protein intensity, protein localization, cell morphology, and fiber texture. This heatmap was organized on treatment and feature axes by agglomerative hierarchical clustering. B) Principal component scores of experimental data reduced to a set of 18 representative fibroblast features. C) Principal component loadings the reduced of PCA scores and loadings define a primary axis of fibroblast activation with correlated protein expression of procollagen, αSMA, and F-actin that is modulated by many drugs. Off-axis, the Src inhibitor WH-4-023 modulated the cell texture feature Actin Long Angular Second Moment, which motivated further study.

219 that drugs induce phenotypic changes distinct from a simple reversal of TGFβ's effects. To
220 further investigate drug-induced changes in phenotype, we analyzed the PCA scores and
221 loadings to infer links between drugs and the features they regulate. Notably, the Src inhibitor
222 WH-4-023 (WH) showed directionality on the scores plot similar to that of Actin Long Angular
223 Second Moment (Actin Long ASM, a measure for F-actin uniformity) on the loadings plot. Actin
224 stress fibers, composed of multiple F-actin filaments along with other proteins, contribute to
225 pathological fibrosis and myofibroblast differentiation[36–38]. This feature and treatment pair
226 showed a negative value on PC1 and a positive value on PC2 relative to the TGFβ and control
227 groups, respectively. The similar directionality of WH and Actin Long ASM suggests that Src
228 inhibition may modulate F-actin uniformity.

229 Based on the initial inference from the PCA, we revisited the images from the high-content
230 microscopy experiment. Fibroblasts treated with TGFβ exhibited discrete F-actin stress fibers,
231 and stress fibers were qualitatively reduced when WH-4-023 (WH) was added (Figure 4 A).
232 Quantitative analysis of F-actin uniformity (inversely correlated with stress fibers) using Actin
233 Long Angular Second Moment (ASM) further supported that TGFβ increased and Src inhibitor
234 WH reduced F-actin uniformity (Figure 4 B).

235 To predict the signaling pathways that specifically regulate F-actin stress fibers, we again
236 applied the LogiMML coupled modeling approach, but this time training the ridge regression
237 layer of the model on experimental measurements of Actin Long ASM. The LogiMML model
238 regression coefficients predicted that the 'Mechanical' module was the top positive regulator of
239 Actin Long ASM and that the 'PI3K' module was the top negative regulator of Actin Long ASM
240 (Figure 4 C). To identify which individual signaling nodes within these two modules most
241 regulate Actin Long ASM, we performed a virtual knockdown screen of the LogiMML network
242 model for regulators of Actin Long ASM in the context of 'TGFβ+WH-4-023' and predicted that
243 Rho, MKK4, and Akt are proximal regulators of Actin Long ASM and actin stress fiber formation
244 (Figure 4 D-E).

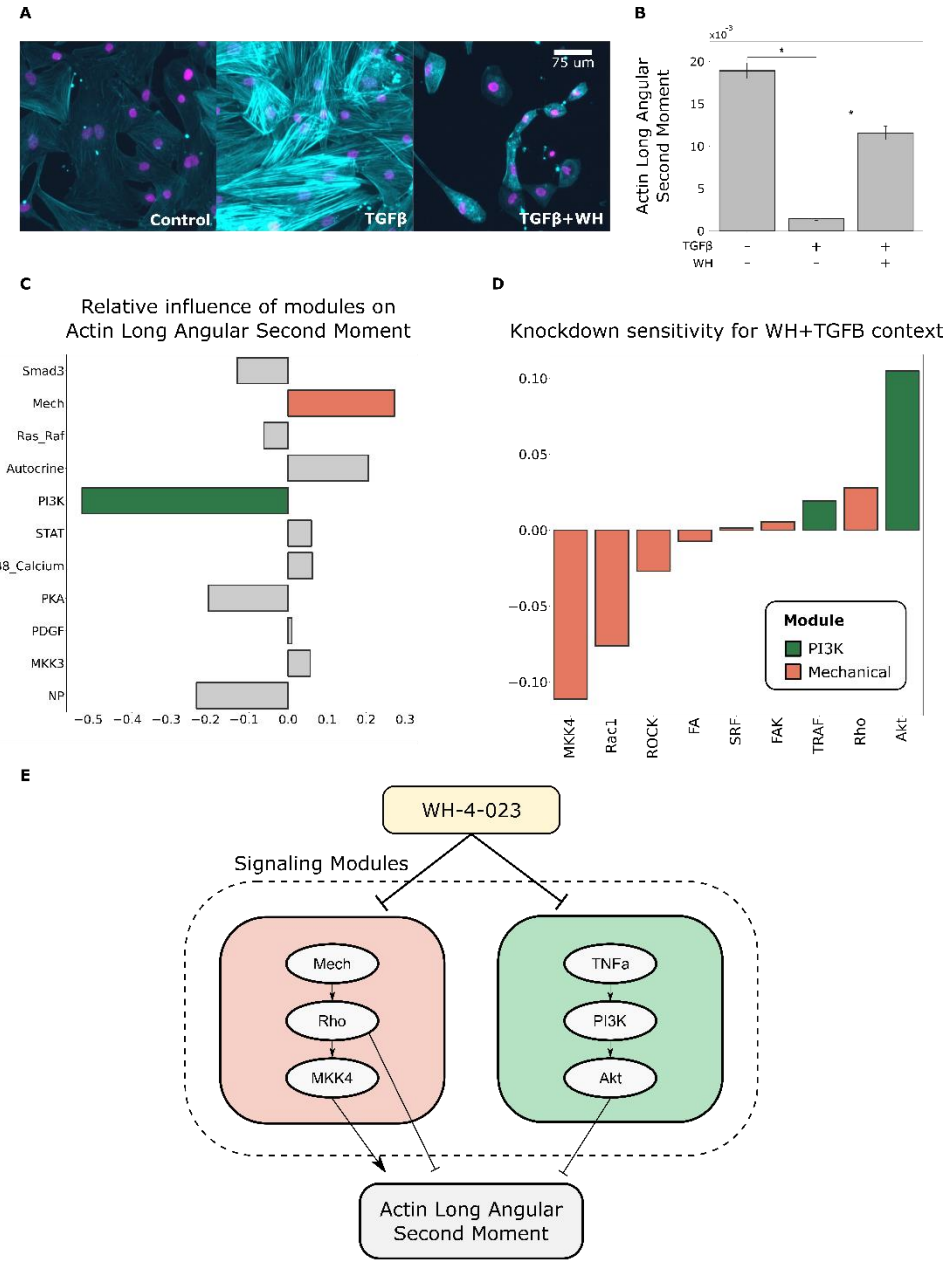
A
75 um
Control
TGFβ
TGFβ+WH
B
Actin Long Angular Second Moment
TGFβ
WH
C
Relative influence of modules on Actin Long Angular Second Moment
Smad3
Mech
Ras_Raf
Autocrine
PI3K
STAT
P38_Calcium
PKA
PDGF
MKK3
NP
D
Knockdown sensitivity for WH+TGFB context
Module
PI3K
Mechanical
MKK4
Rac1
ROCK
FA
SRF
FAK
TRAF
Rho
Akt
E
WH-4-023
Signaling Modules
Mech
Rho
MKK4
TNFa
PI3K
Akt
Actin Long Angular Second Moment

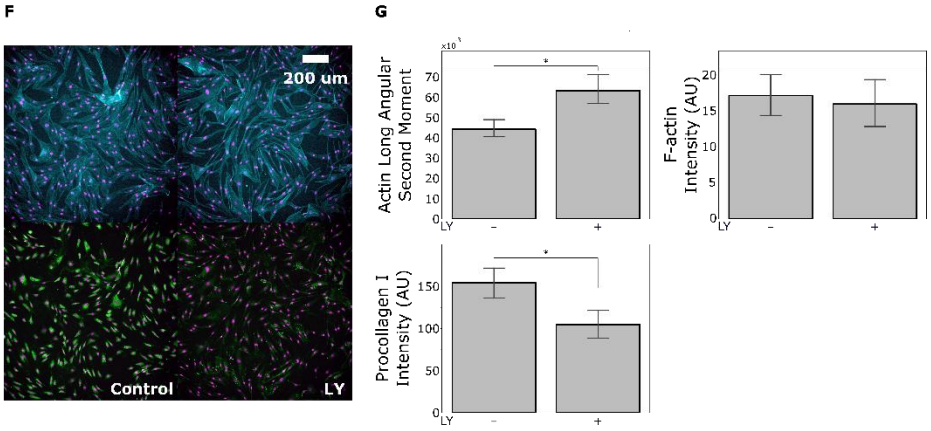
F
200 um
Control
LY
G
Actin Long Angular Second Moment
F-actin Intensity (AU)
Procollagen I Intensity (AU)

245

246

Figure 4: **Logic-based mechanistic machine learning predicts the PI3K module to mediate how Src inhibitor suppresses stress fibers, validated by subsequent experiments.** A) Images of human cardiac fibroblasts treated with baseline control stimulus, TGFβ, or TGFβ + WH-4-023. B) Quantification of Actin Long Angular Second Moment (ASM), a measure of F-actin uniformity and reduced stress fibers based on images in panel A. C) Regression coefficients from the LogiMML mechanistic machine learning model that predicts network modules that regulate actin long ASM. D) Knockdown sensitivity analysis predicting individual proteins that regulate actin long ASM in the TGFβ+WH-4-023 signaling context. E) Signaling schematic for WH-4-023 effect on actin long ASM, derived from sensitivity analysis in panel D. F) Human cardiac fibroblasts treated with PI3K inhibitor LY294002 or baseline control stimulus, measuring F-actin and procollagen expression. G) Quantification of long actin Angular Second Moment (measure of F-actin uniformity), F-actin integrated intensity, and Procollagen I integrated intensity. *p≤0.05 ANOVA with Tukey's post-hoc in panel B, and *p≤0.05 Student's T-test in panel G.

247 ### PI3K signaling stimulates F-actin stress fiber formation and collagen expression

248 After deriving a putative signaling schematic for Actin Long ASM using the LogiMML model, we
249 aimed to experimentally validate the prediction that inhibition of PI3K/Akt would suppress
250 stress fiber formation and thereby increase Actin Long ASM (Figure 4 E). In previous studies
251 using PI3K inhibitors, PI3K was shown to regulate fibroblast contractility, fibroblast-to-
252 myofibroblast transition, and TGFβ-induced αSMA and collagen production[39,40]. Given these
253 previously implicated roles for PI3K in myofibroblast activation and fibrosis, we investigated if
254 PI3K regulates F-actin stress fiber formation in cardiac fibroblasts. We treated human cardiac
255 fibroblasts with either a negative control condition or a 20 μM dose of the PI3K inhibitor
256 LY294002 (LY). Treatment with LY significantly increased Actin Long ASM, but notably, it had no
257 significant effect on the total assembly of F-actin in each cell, measured by integrated F-actin
258 intensity (Figure 4 F-G). This selective effect of PI3K inhibition on stress fiber formation, while
259 having no significant effect on total F-actin, suggests that F-actin assembly and stress fiber
260 formation are differentially regulated processes. PI3K inhibition also significantly reduced
261 integrated procollagen I intensity, demonstrating a role for PI3K signaling in cardiac fibroblast
262 collagen production (Figure 4G).

263 ## Discussion

264 Cardiac fibroblasts are central regulators and promising therapeutic targets following cardiac
265 injury. To identify how clinically relevant drugs regulate diverse aspects of fibroblast
266 phenotype, we performed high-content screening of 13 drugs in 4 environmental contexts. We
267 expanded our high-content microscopy feature set to 137 single-cell features, measuring
268 fibrotic marker protein intensity, intracellular protein distribution, fiber texture, and cell
269 morphology. After reducing the feature space and dimensionality of our experimental data, we
270 found that many aspects of fibroblast phenotype are uniquely induced by drug and cytokine
271 treatments. Notably, when administered with TGFβ, the drugs WH-4-023, defactinib, fasudil,
272 and pirfenidone induced phenotypes that deviated from the PCA axis corresponding to classical

273 TGFβ response. The differences between these phenotypes can be partially explained by
274 differential drug regulation of features capturing procollagen I and αSMA expression, and F-
275 actin assembly and stress fiber formation. To predict how drugs regulate cell signaling and
276 influence phenotype, we developed the logic-based mechanistic machine learning (LogiMML)
277 approach which coupled the logic-based fibroblast network model with a ridge regression
278 model trained on the high-content drug screen. Using this expanded LogiMML model, we
279 predicted regulatory mechanisms for pirfenidone and Src inhibitor WH-4-023 on F-actin. We
280 predicted that pirfenidone regulates F-actin assembly via the 'P38_Calcium', 'Smad3', and 'PI3K'
281 signaling modules, with Akt, p38, and CBP predicted to be positive drivers of F-actin assembly
282 within these modules. We also predicted that WH-4-023 regulates F-actin stress fiber formation
283 via the 'PI3k' and 'Mechanical' signaling modules. As predicted by the LogiMML model, we
284 experimentally validated that PI3K inhibition reduces F-actin stress fiber formation in human
285 cardiac fibroblasts. These studies validate the ability of the LogiMML approach to predict
286 signaling mechanisms from a phenotypic screen.

287 Differential regulation of fibroblast phenotype by drugs and the development of targeted 288 antifibrotic therapies

289 Drugs that specifically target fibroblast signaling may provide directed control over the fibrotic
290 response. A major challenge in therapeutic development for fibrosis is that many drugs capable
291 of reducing fibrosis target non-specific regulatory pathways outside of the fibrotic response. For
292 example, the ALK5 inhibitor galunisertib targets the TGFβ receptor and shows promising
293 therapeutic reduction of fibrosis across organs[41–43]. While TGFβ receptor inhibition can reduce
294 fibrosis, recent efforts in target discovery have successfully identified new approaches to
295 mitigate fibrosis that are more fibroblast specific. For example, it was shown that activating
296 fibroblast-specific TLR4 in mice can drive the development of skin and lung fibrosis and that
297 TLR4 inhibition reduces αSMA expression and collagen production in fibroblasts [44]. Another
298 study showed that fibroblast-specific knockout of STAT3 ameliorates skin fibrosis, and that
299 pharmacological inhibition of STAT3 successfully reduces myofibroblast activation, collagen
300 accumulation, and dermal thickening in experimental fibrosis in mice[45]. Future work can
301 advance our understanding of how candidate drugs regulate specific components of the fibrotic
302 response in fibroblasts and provide targeted control of fibrosis.

303 Features of cardiac fibroblast phenotype

304 Following the reduction of the original set of 137 single-cell features from our high content
305 image analysis, we identified a set of 18 phenotypic features of fibroblasts that exhibit high
306 heterogeneity in response to drug treatments (Figure S 2, Table S 2). Notably, many of the
307 features measuring fiber texture for αSMA and F-actin show different response patterns
308 compared to features measuring overall expression level for those respective proteins (i.e.
309 aSMA integrated intensity versus aSMA long correlation). This distribution of features indicates
310 that the expression and organization of aSMA and F-actin are independently regulated by
311 candidate drugs. The processes of αSMA protein expression and fiber assembly have different

312 degrees of contribution to pathological fibrosis. For example, a recent study showed that
313 fibroblasts can compensate for the loss of *Acta2* transcription and form stress fibers using
314 similar proteins, implying that stress fiber formation is more important than αSMA production
315 for the fibrotic response[46]. Incorporating an expanded set of measurements in future fibrosis
316 studies may provide greater resolution of the fibrotic phenotype in response to therapies and
317 help evaluate changes in pathologically relevant features beyond protein expression.

318 Contributions of the LogiMML mechanistic machine learning approach

319 Mechanistic logic-based differential equation models have enabled systematic prediction of
320 drug action, yet these models are limited by the availability of priori knowledge [13,47–49]. An
321 alternative is machine learning, although 'black-box' ML approaches like artificial neural
322 networks predict input-output relationships without mechanistic insight. In contrast, two recent
323 studies combined mechanistic modeling with machine learning models like regression and
324 visible neural networks to predict antibiotic stress on metabolism and drug synergies for
325 cancer[29,50]. These 'white-box' approaches provide greater transparency of the intermediate
326 layers between input and output[51].

327 Building on such advances for logic-based biological networks, our LogiMML mechanistic
328 machine learning approach combines the flexible trainability of a machine learning model with
329 the robust experimentally-determined internal network structure of a mechanistic model. In
330 this study, we used the LogiMML model to predict signaling mechanisms that mediate how
331 drugs regulate F-actin assembly and stress fiber formation in cardiac fibroblasts. However, this
332 is just one of many possible applications for this modeling framework. The LogiMML approach
333 is designed to work across multiple mechanistic modeling formalisms and types of experimental
334 data, coupling the mechanistic model and data to predict mechanisms for the phenotype of
335 interest. The flexible nature of LogiMML presents promising future applications to elucidate cell
336 signaling that regulates diverse cellular phenotypes.

337 Src kinase as a therapeutic target for fibrosis

338 Of the 13 drugs used in this study, the Src inhibitor WH-4-023 (WH) was one of three drugs that
339 showed a strong reversal in TGFβ-induced F-actin, αSMA, and procollagen I expression. WH was
340 also effective at reversing the formation of F-actin stress fibers in response to TGFβ. Src
341 inhibitors dasatinib, ponatinib, and saracatinib have all been used in clinical trials across
342 different types of cancer[52–56]. In cancer, Src has been shown to promote proliferation and
343 metastasis through many signaling targets including FAK, Akt, Ras, and PI3K[57–61].

344 Given that Src signaling affects many central regulatory pathways, recent studies have tested
345 the potential for Src inhibition as a therapy for fibrotic disease. In a renal fibrosis study, blocking
346 Src kinase using PP1 was shown to inhibit TGFβ-induced expression of collagen I, αSMA, and
347 fibronectin[62]. In that study, Src inhibition was also shown the reduce the development of renal
348 fibrosis in obstructed kidneys *in vivo* in mice, indicating Src inhibition as a potential renal
349 fibrosis and chronic kidney disease therapy. Another study focusing on lung fibrosis showed

350 that TGFβ induces Src kinase activity in lung fibroblasts and that Src is required for
351 myofibroblast contraction[63]. Further, inhibition of Src kinase *in vivo* with AZD0530 reduced scar
352 area and αSMA expression in mice with bleomycin-induced lung fibrosis[63].

353 In this study, we applied the LogiMML network to investigate how Src contributes to F-actin
354 stress fiber formation induced by TGFβ. We predicted that PI3K signaling contributes to
355 profibrotic Src signaling in cardiac fibrosis. This proposed mechanism is supported by previous
356 studies, showing that PI3K regulates fibroblast contractility and myofibroblast activation in skin
357 fibroblasts, and TGFβ-induced αSMA and collagen production in lung fibroblasts[39,40]. To validate
358 this proposed profibrotic role for PI3K, we show that PI3K inhibition reduced procollagen I
359 production and F-actin stress fiber organization in HCFs. While previous work has shown that
360 mechanical stretch, Rho-kinase, and myosin light chain kinase (MLCK) positively regulate the
361 organization of F-actin filaments into stress fibers, the role of PI3K's regulation of F-actin stress
362 fiber formation has not been thoroughly explored[64,65]. Here, we show that treatment with PI3K
363 inhibitor LY294002 (LY) significantly reduces stress fiber formation without affecting the total
364 amount of assembled F-actin, implying PI3K specifically enhances stress fiber formation in
365 cardiac fibroblasts. Future studies should explore if Src kinase inhibitors mitigate cardiac fibrosis
366 *in vivo*, and to what degree PI3K kinase contributes to the regulation of cardiac fibrosis by Src.

367 Limitations and future directions

368 The main limitation of this study is that our modeling and experimental approaches address cell
369 signaling in cardiac fibroblasts *in vitro*, but do not address how fibroblasts respond to drugs in
370 an *in vivo* signaling environment. Our experimental data also captures some key fibrotic
371 proteins, but does not measure other fibrotic outputs of interest, like EDA fibronectin, and does
372 not capture a comprehensive signaling profile of the fibroblast. Despite these limitations, the
373 LogiMML framework was sufficient to predict a validated role for PI3K in promoting stress fiber
374 formation. Experimentally, future work could include proteomics or RNA-seq analysis of
375 fibroblasts to measure how drugs differentially regulate intracellular molecular profiles. Future
376 modeling work could include simulated conditions for *in vivo* or *in vitro* co-culture conditions to
377 incorporate the signaling influence of other cell types. Given the flexibility of the LogiMML
378 modeling approach, these simulated data could be feasibly paired with respective experimental
379 data to make predictions for fibroblast signaling under new conditions.

380 Conclusions

381 In this study, we showed that drugs differentially regulate cardiac fibroblast phenotype and
382 work via distinct mechanisms that can be predicted by logic-based mechanistic machine
383 learning. By expanding the microscopy feature set in the high content imaging pipeline, we
384 captured greater resolution of the fibroblast phenotype and measured how phenotypic
385 features changed in response to drugs. Using our LogiMML modeling approach, we predicted
386 signaling mechanisms for how pirfenidone and Src inhibitor WH-4-023 affect F-actin protein
387 assembly and stress fiber formation, respectively. We predicted that PI3K regulates F-actin
388 stress fiber formation, which we experimentally validated in human cardiac fibroblasts. This

389 study presents new features of fibroblast phenotype to be further explored in fibrosis,
390 identifies specific roles for PI3K in cardiac fibroblast signaling, and demonstrates an adaptable
391 mechanistic machine learning approach to predict signaling outcomes for fibrosis that can be
392 expanded to other diseases.

393

394 Methods

395 *In vitro* experiments in human cardiac fibroblasts

396 Primary human ventricular cardiac fibroblasts were purchased from PromoCell (PromoCell C-
397 12375; PromoCell GmbH, Germany). Cells were cultured in DMEM containing 10% FBS and 1%
398 Pen/Strep, and were kept in an incubator maintained at 5% CO_2. Cells were plated in a 96-well
399 plate at 5,000 cells/well and then grown in 10% FBS for 24 hours, serum starved for 24 hours,
400 and then treated with the following cytokine conditions for 96 hours: 0% FBS control media, 0%
401 FBS media with 20ng/mL TGFβ1 (Cell Signaling Technology, 8915LC), and 0% FBS media with 10
402 ng/mL human IL1β (Cell Signaling Technology, 8900SC), or TGFβ1 and IL1β combined. Cells were
403 treated with these conditions either alone or with 1 of 13 compounds at 1 of 3 concentrations.
404 We determined drug concentrations via a literature search, prioritizing concentrations that
405 yielded significant effects *in vitro* in fibroblasts or similar cell types. The drugs with their
406 respective concentrations are as follows: [0.25,1,2] µg/ml of anakinra (Kineret, SOBI Inc.),
407 [1,5,10] µM valsartan (Sigma-Aldrich, SML0142-10MG), [0.2,1,2] µM BNP (Sigma-Aldrich,
408 B5900-.5MG), [1,5,10]µM valsartan combos respectively with [0.2,1,2] µM BNP, [10,30,60]mM
409 glutathione (Sigma-Aldrich, G4251-1G), [1,3,5] µM CW-HM12 (Cayman Chemical Company,
410 19480), [10,20,50] µM salbutamol (Sigma-Aldrich, S8260-25MG), [5,10,25] µM marimistat
411 (Sigma-Aldrich, M2699-5Mg), [1,5,10] µM galunisertib (Selleck Chemicals, S2230), [12.5,25,50]
412 µM fasudil (Sigma-Aldrich, CDS021620-10MG), [10,25,50]µM SB203580 (Sigma-Aldrich, S8307-
413 1MG), [1,5,10] mg/mL pirfenidone (Sigma-Aldrich, P2116-10MG), [5,10,20] µM defactinib
414 (MedChem Express, HY-12289A), [5,10,20] µM WH-4-023 (Sigma-Aldrich, SML1334-5MG), and
415 20 µM LY294002 (Selleck Chemicals, S1105). Cells were grown in these conditions for 72 hours.

416 Cells were then fixed in 4% PFA in PBS for 30 minutes, permeabilized and blocked for 1 hour in
417 a solution containing 3% BSA and 0.2% Triton, and then stained overnight at 4°C with a 1:500
418 Anti-Collagen I antibody (Abcam, ab34710). After overnight incubation, cells were washed 3x in
419 PBS and stained with 1:5000 Dapi, 1:1000 Phalloidin CruzFluor 647 Conjugate (Santa Cruz
420 Biotechnology, sc-363797), 1:250 α-Smooth Muscle Actin antibody (Sigma-Aldrich, C6198), and
421 1:1000 Goat-anti-Rabbit (ThermoFisher Scientific, A-11034).

422 Microscopy and single-cell quantification

423 96-well plates we imaged using the Operetta CLS High-Content Analysis System (Perkin Elmer).
424 All three replicate wells for each condition were imaged and quantified. To quantify αSMA
425 expression, an automated image analysis pipeline was employed in CellProfiler (Broad
426 Institute)[22]. Fibroblast nuclei were identified by the DAPI signal. Next, the collagen-positive

region corresponding to each nucleus was segmented using the "propagate" algorithm, using the segmented nucleus as the seed. Next, Fibroblast boundaries were segmented using the "propagate" algorithm, musing the segmented collagen region as the seed. αSMA signal was integrated within each cell's boundary. Short, medium, and long texture feature information was derived using the MeasureTexture module in CellProflier using texture scales of 2, 6, and 10 pixels respectively. Texture feature values were calculated by subtracting the smallest angle value of a given feature from the largest angle value of that same feature for each cell. F-actin and procollagen expressions were quantified similarly.

Statistics

Feature values for each well were determined by taking the median value of the feature across all cells in the center tile of each well. Well median values were used as replicates (n=3). Significance was determined using an ANOVA with Tukey's posthoc in comparisons between more than two groups, and Student's T-test in comparisons between two groups. Automated data analysis and statistical calculations were performed using Python 3.8.5 and the 'statsmodels' Python module version 0.13.2.

Model Simulations

Drug simulations in the fibroblast network model were performed as previously described using MATLAB version 2022a[12,13,66]. Predicted node activity is calculated using logic-based Hill differential equations. Agonist and antagonist drug relationships were represented by altering the activation function of the target node, representing either competitive or non-competitive drug interactions with the respective target. To better represent the cell-to-cell variability observed in *in vitro* cell responses to treatments, we employed a previously developed ensemble modeling approach combining multiple simulations with random normally distributed parameters[66]. Ensemble simulations were performed using the MATLAB 'normrnd' function from the 'Statistics and Machine Learning' toolbox to randomly sample parameters within a normal distribution and simulation n of 100. The randomly sampled parameters and means of the sampling ranges are as follows: baseline ligand inputs (0.25), mechanical input (0.85), drug dose (0.85), and raised ligand inputs (0.6). The sampling range for each parameter was calculated by $paramMean \pm COV * paramMean$ where COV=0.0396. This COV value, used to scale stochasticity in the model was determined by taking the average coefficient of variation in F-actin, procollagen I, and αSMA expression in human cardiac fibroblasts treated with TGFβ from our *in vitro* experiments.

LogiMML Network-Regression Coupling

The LogiMML mechanistic machine learning model is comprised of a network model layer and a Ridge regression layer. The independent 'X' variables used to train the regression model are node activity values from the network model predicted under each simulated drug and environmental condition. To reduce model complexity, network nodes were clustered into 11 signaling modules derived from k-means clustering on a combined sensitivity and influence analysis on the network model[12]. The node activity values were averaged within each module,

466 and these modules' mean activity values were fed into the regression layer. The dependent 'Y'
467 variables for this model were experimentally measured values from our high-content imaging
468 experiments in human cardiac fibroblasts. Sensitivity knockout analysis was performed by
469 simulating a given drug and cytokine context int network model i.e. 'TGFβ+pirfenidone' and
470 sequentially setting each node ymax value to 0, measuring reduction or increase in the
471 dependent variable e.g. 'F-actin Intensity' upon knockdown. Leave-one-out cross validation
472 (LOOCV) was performed on the LogiMML model to evaluate performance across variations in
473 the experimental data set. The means and standard deviations of the LOOCV MSE values were
474 0.022 and 0.080 for the F-actin Intensity model and 0.083 and 0.142 for the Long Actin ASM
475 model.

476

477 ## Acknowledgements

478 We acknowledge Dr. Sarah Ewald at the University of Virginia Carter Immunology Center for
479 providing anakinra used in this study.

480

481 ## Funding

482 This study was funded by the NIH (HL137755, HL007284, HL160665, HL162925, 1S10OD021723-
483 01A1).

484

485 ## References

486 1. Burgos Villar, K. N., Liu, X. & Small, E. M. Transcriptional regulation of cardiac fibroblast
487 phenotypic plasticity. *Curr. Opin. Physiol.* **28**, 100556 (2022).

488 2. Jacobs, A. K. *et al.* Systems of Care for ST-Segment-Elevation Myocardial Infarction: A
489 Policy Statement From the American Heart Association. *Circulation* **144**, e310–e327
490 (2021).

491 3. Burke, R. M., Lighthouse, J. K., Mickelsen, D. M. & Small, E. M. Sacubitril/Valsartan
492 Decreases Cardiac Fibrosis in Left Ventricle Pressure Overload by Restoring PKG Signaling
493 in Cardiac Fibroblasts. *Circ. Hear. Fail.* **12**, (2019).

494 4. Fan, Z. & Guan, J. Antifibrotic therapies to control cardiac fibrosis. *Biomater. Res. 2016*
495 *201* **20**, 1–13 (2016).

496 5. Welch, M. P., Odland, G. F. & Clark, R. A. F. Temporal relationships of F-actin bundle
497 formation, collagen and fibronectin matrix assembly, and fibronectin receptor expression
498 to wound contraction. *J. Cell Biol.* **110**, 133–145 (1990).

499 6. Travers, J. G., Kamal, F. A., Robbins, J., Yutzey, K. E. & Blaxall, B. C. Cardiac Fibrosis: The
500 Fibroblast Awakens. *Circ. Res.* **118**, 1021–40 (2016).

501 7. Sun, K. H., Chang, Y., Reed, N. I. & Sheppard, D. α-smooth muscle actin is an inconsistent
502 marker of fibroblasts responsible for force-dependent TGFβ activation or collagen
503 production across multiple models of organ fibrosis. *Am. J. Physiol. - Lung Cell. Mol.*
504 *Physiol.* **310**, L824–L836 (2016).

505 8. Avery, D. *et al.* Extracellular Matrix Directs Phenotypic Heterogeneity of Activated
506 Fibroblasts. *Matrix Biol.* **67**, 90 (2018).

507 9. Deng, C. C. *et al.* Single-cell RNA-seq reveals fibroblast heterogeneity and increased
508 mesenchymal fibroblasts in human fibrotic skin diseases. *Nat. Commun. 2021 121* **12**, 1–
509 16 (2021).

510 10. Gerckens, M. *et al.* Phenotypic drug screening in a human fibrosis model identified a
511 novel class of antifibrotic therapeutics. *Sci. Adv.* **7**, 3673 (2021).

512 11. Fu, X. *et al.* Specialized fibroblast differentiated states underlie scar formation in the
513 infarcted mouse heart. *J. Clin. Invest.* **128**, 2127–2143 (2018).

514 12. Zeigler, A. C., Richardson, W. J., Holmes, J. W. & Saucerman, J. J. A computational model
515 of cardiac fibroblast signaling predicts context-dependent drivers of myofibroblast
516 differentiation. *J. Mol. Cell. Cardiol.* **94**, 72–81 (2016).

517 13. Zeigler, A. C. *et al.* Network model-based screen for FDA-approved drugs affecting
518 cardiac fibrosis. *CPT Pharmacometrics Syst. Pharmacol.* **10**, 377–388 (2021).

519 14. Kort, E. & Jovinge, S. Drug Repurposing: Claiming the Full Benefit from Drug
520 Development. *Curr. Cardiol. Rep.* **23**, 1–7 (2021).

521 15. Abdelsayed, M., Kort, E. J., Jovinge, S. & Mercola, M. Repurposing drugs to treat
522 cardiovascular disease in the era of precision medicine. doi:10.1038/s41569-022-00717-6

523 16. Khalil, H. *et al.* Fibroblast-specific TGF-β-Smad2/3 signaling underlies cardiac fibrosis. *J.*
524 *Clin. Invest.* **127**, 3770–3783 (2017).

525 17. Turner, N. A. *et al.* Interleukin-1α stimulates proinflammatory cytokine expression in
526 human cardiac myofibroblasts. *Am. J. Physiol. Circ. Physiol.* **297**, H1117–H1127 (2009).

527 18. Francis Stuart, S. D., De Jesus, N. M., Lindsey, M. L. & Ripplinger, C. M. The crossroads of
528 inflammation, fibrosis, and arrhythmia following myocardial infarction. *J. Mol. Cell.*
529 *Cardiol.* **91**, 114–22 (2016).

530 19. Deten, A., Volz, H. C., Briest, W. & Zimmer, H.-G. Cardiac cytokine expression is
531 upregulated in the acute phase after myocardial infarction. Experimental studies in rats.
532 *Cardiovasc. Res.* **55**, 329–340 (2002).

533 20. Bujak, M., Frangogiannis, N. G. & Hirszfeld, © L. The role of IL-1 in the pathogenesis of
534 heart disease THE IL−1 FAMILY OF CYTOKINES. doi:10.1007/s00005-009-0024-y

535 21. BUJAK, M. & FRANGOGIANNIS, N. The role of TGF-β signaling in myocardial infarction and
536 cardiac remodeling. *Cardiovasc. Res.* **74**, 184–195 (2007).

537 22. Stirling, D. R. *et al.* CellProfiler 4: improvements in speed, utility and usability. *BMC*
538 *Bioinformatics* **22**, 1–11 (2021).

539 23. Abbate, A. *et al.* Effects of interleukin-1 blockade with anakinra on adverse cardiac
540 remodeling and heart failure after acute myocardial infarction [from the virginia
541 commonwealth university-anakinra remodeling trial (2) (vcu-art2) pilot study]. *Am. J.*
542 *Cardiol.* **111**, (2013).

543 24. Abbate, A. *et al.* Anakinra, a recombinant human interleukin-1 receptor antagonist,
544 inhibits apoptosis in experimental acute myocardial infarction. *Circulation* **117**, (2008).

545 25. Abbate, A. *et al.* Interleukin-1 blockade inhibits the acute inflammatory response in
546 patients with st-segment–elevation myocardial infarction. *J. Am. Heart Assoc.* **9**, (2020).

547 26. Bracco Gartner, T. C. L. *et al.* Pirfenidone Has Anti-fibrotic Effects in a Tissue-Engineered
548 Model of Human Cardiac Fibrosis. *Front. Cardiovasc. Med.* **9**, 459 (2022).

549 27. Behr, J. *et al.* Pirfenidone in patients with progressive fibrotic interstitial lung diseases
550 other than idiopathic pulmonary fibrosis (RELIEF): a double-blind, randomised, placebo-
551 controlled, phase 2b trial. *Lancet Respir. Med.* **9**, 476–486 (2021).

552 28. Sandbo, N. & Dulin, N. The actin cytoskeleton in myofibroblast differentiation:
553 Ultrastructure defining form and driving function. *Transl. Res.* **158**, 181 (2011).

554 29. Yang, J. H. *et al.* A White-Box Machine Learning Approach for Revealing Antibiotic
555 Mechanisms of Action. *Cell* **177**, 1649-1661.e9 (2019).

556 30. Rieg, T., Frick, J., Baumgartl, H. & Buettner, R. Demonstration of the potential of white-
557 box machine learning approaches to gain insights from cardiovascular disease
558 electrocardiograms. *PLoS One* **15**, e0243615 (2020).

559 31. McNeish, D. M. Using Lasso for Predictor Selection and to Assuage Overfitting: A Method
560 Long Overlooked in Behavioral Sciences. *Multivariate Behav. Res.* **50**, 471–484 (2015).

561 32. Hu, T. *et al.* Reactive oxygen species production via NADPH oxidase mediates TGF-β-
562 induced cytoskeletal alterations in endothelial cells. *Am. J. Physiol. - Ren. Physiol.* **289**,
563 816–825 (2005).

564 33. Huot, J. *et al.* SAPK2/p38-dependent F-Actin Reorganization Regulates Early Membrane
565 Blebbing during Stress-induced Apoptosis. *J. Cell Biol.* **143**, 1361–1373 (1998).

566 34. Qian, Y. *et al.* PI3K induced actin filament remodeling through Akt and p70S6K1:
567 implication of essential role in cell migration. *Am. J. Physiol. Cell Physiol.* **286**, (2004).

568 35. Haralick, R. M., Dinstein, I. & Shanmugam, K. Textural Features for Image Classification.
569 *IEEE Trans. Syst. Man Cybern.* **SMC-3**, 610–621 (1973).

570 36. Nagaraju, C. K. *et al.* Myofibroblast Phenotype and Reversibility of Fibrosis in Patients
571 With End-Stage Heart Failure. *J. Am. Coll. Cardiol.* **73**, 2267–2282 (2019).

572 37. Sandbo, N. *et al.* Delayed stress fiber formation mediates pulmonary myofibroblast

573 differentiation in response to TGF-β. *Am. J. Physiol. - Lung Cell. Mol. Physiol.* **301**, 656–
574 666 (2011).

575 38. Naumanen, P., Lappalainen, P. & Hotulainen, P. Mechanisms of actin stress fibre
576 assembly. *J. Microsc.* **231**, 446–454 (2008).

577 39. Conte, E. *et al.* Inhibition of PI3K prevents the proliferation and differentiation of human
578 lung fibroblasts into myofibroblasts: The role of class I P110 isoforms. *PLoS One* **6**, (2011).

579 40. Li, G., Li, Y. Y., Sun, J. E., Lin, W. H. & Zhou, R. X. ILK-PI3K/AKT pathway participates in
580 cutaneous wound contraction by regulating fibroblast migration and differentiation to
581 myofibroblast. *Lab. Investig.* **96**, 741–751 (2016).

582 41. Luangmonkong, T. *et al.* Evaluating the antifibrotic potency of galunisertib in a human ex
583 vivo model of liver fibrosis. *Br. J. Pharmacol.* **174**, (2017).

584 42. Masuda, A. *et al.* Promotion of liver regeneration and anti-fibrotic effects of the TGF-β
585 receptor kinase inhibitor galunisertib in CCl4-treated mice. *Int. J. Mol. Med.* **46**, (2020).

586 43. Dadrich, M. *et al.* Combined inhibition of TGFβ and PDGF signaling attenuates radiation-
587 induced pulmonary fibrosis. *Oncoimmunology* **5**, (2016).

588 44. Bhattacharyya, S. *et al.* TLR4-dependent fibroblast activation drives persistent organ
589 fibrosis in skin and lung. *JCI insight* **3**, (2018).

590 45. Chakraborty, D. *et al.* Activation of STAT3 integrates common profibrotic pathways to
591 promote fibroblast activation and tissue fibrosis. *Nat. Commun. 2017 81* **8**, 1–16 (2017).

592 46. Li, Y. *et al.* Loss of Acta2 in cardiac fibroblasts does not prevent the myofibroblast
593 differentiation or affect the cardiac repair after myocardial infarction. *J. Mol. Cell.*
594 *Cardiol.* **171**, 117–132 (2022).

595 47. Tan, P. M., Buchholz, K. S., Omens, J. H., McCulloch, A. D. & Saucerman, J. J. Predictive
596 model identifies key network regulators of cardiomyocyte mechano-signaling. *PLoS*
597 *Comput. Biol.* **13**, (2017).

598 48. Ryall, K. A. *et al.* Network reconstruction and systems analysis of cardiac myocyte
599 hypertrophy signaling. *J. Biol. Chem.* **287**, 42259–42268 (2012).

600 49. Kraeutler, M. J., Soltis, A. R. & Saucerman, J. J. Modeling cardiac β-adrenergic signaling
601 with normalized-Hill differential equations: comparison with a biochemical model. *BMC*
602 *Syst. Biol.* **4**, 157 (2010).

603 50. Kuenzi, B. M. *et al.* Predicting Drug Response and Synergy Using a Deep Learning Model
604 of Human Cancer Cells. *Cancer Cell* **38**, 672-684.e6 (2020).

605 51. Petch, J., Di, S. & Nelson, W. Opening the Black Box: The Promise and Limitations of
606 Explainable Machine Learning in Cardiology. *Can. J. Cardiol.* **38**, 204–213 (2022).

607 52. Belli, S. *et al.* C-Src and EGFR inhibition in molecular cancer therapy: What else can we
608 improve? *Cancers* **12**, (2020).

609 53. Gucalp, A. *et al.* Phase II trial of saracatinib (AZD0530), an oral SRC-inhibitor for the
610 treatment of patients with hormone receptor-negative metastatic breast cancer. *Clin.*
611 *Breast Cancer* **11**, (2011).

612 54. Cortes, J. *et al.* Ponatinib dose-ranging study in chronic-phase chronic myeloid leukemia:
613 a randomized, open-label phase 2 clinical trial. *Blood* **138**, (2021).

614 55. Haura, E. B. *et al.* Phase I/II study of the Src inhibitor dasatinib in combination with
615 erlotinib in advanced non-small-cell lung cancer. *J. Clin. Oncol.* **28**, (2010).

616 56. Twardowski, P. W. *et al.* A phase II trial of dasatinib in patients with metastatic
617 castration-resistant prostate cancer treated previously with chemotherapy. *Anticancer.*
618 *Drugs* **24**, (2013).

619 57. Beadnell, T. C. *et al.* Src-mediated regulation of the PI3K pathway in advanced papillary
620 and anaplastic thyroid cancer. *Oncogenesis* **7**, (2018).

621 58. Bunda, S. *et al.* Src promotes GTPase activity of Ras via tyrosine 32 phosphorylation.
622 *Proc. Natl. Acad. Sci. U. S. A.* **111**, (2014).

623 59. Xiao, X. *et al.* Diallyl disulfide suppresses SRC/Ras/ERK signaling-mediated proliferation
624 and metastasis in human breast cancer by up-regulating miR-34a. *PLoS One* **9**, (2014).

625 60. Westhoff, M. A., Serrels, B., Fincham, V. J., Frame, M. C. & Carragher, N. O. Src-Mediated
626 Phosphorylation of Focal Adhesion Kinase Couples Actin and Adhesion Dynamics to
627 Survival Signaling. *Mol. Cell. Biol.* **24**, (2004).

628 61. Mahajan, K. & Mahajan, N. P. PI3K-independent AKT activation in cancers: A treasure
629 trove for novel therapeutics. *Journal of Cellular Physiology* **227**, (2012).

630 62. Yan, Y. *et al.* Src inhibition blocks renal interstitial fibroblast activation and ameliorates
631 renal fibrosis. *Kidney Int.* **89**, (2016).

632 63. Hu, M. *et al.* Therapeutic Targeting of Src Kinase in Myofibroblast Differentiation and
633 Pulmonary Fibrosis. *J. Pharmacol. Exp. Ther.* **351**, 87 (2014).

634 64. Katoh, K., Kano, Y., Amano, M., Kaibuchi, K. & Fujiwara, K. Stress fiber organization
635 regulated by MLCK and Rho-kinase in cultured human fibroblasts. *Am. J. Physiol. - Cell*
636 *Physiol.* **280**, (2001).

637 65. Kaunas, R., Nguyen, P., Usami, S. & Chien, S. Cooperative effects of Rho and mechanical
638 stretch on stress fiber organization. *Proc. Natl. Acad. Sci. U. S. A.* **102**, (2005).

639 66. Zeigler, A. C. *et al.* Computational Model Predicts Paracrine and Intracellular Drivers of
640 Fibroblast Phenotype After Myocardial Infarction. *Matrix Biol.* (2020).
641 doi:10.1016/j.matbio.2020.03.007

642

643